





Article

Metal Oxide Nanoparticle-Based Coating as a Catalyst for A-TIG Welding: Critical Raw Material Perspective

Sebastian Balos ^{1,*}, Miroslav Dramicanin ¹, Petar Janjatovic ¹, Ivan Zabunov ²,
Damjan Klobcar ³, Matija Busic ⁴ and Maria Luisa Grilli ⁵

¹ Faculty of Technical Sciences, University of Novi Sad, Trg Dositeja Obradovica 6, 21000 Novi Sad, Serbia; dramicanin@uns.ac.rs (M.D.); janjatovic@uns.ac.rs (P.J.)

² Faculty of Special Technology, Alexander Dubček University of Trenčín, Študentská 2 911 50 Trenčín, Slovakia; ivan.zabunov@tnuni.sk

³ Faculty of Mechanical Engineering, University of Ljubljana, Aškerčeva c. 6, 1000 Ljubljana, Slovenia; Damjan.Klobcar@fs.uni-lj.si

⁴ Faculty of Mechanical Engineering and Naval Architecture, University of Zagreb, Ivana Lučića 5, 10002 Zagreb, Croatia; Matija.Busic@fsb.hr

⁵ Italian National Agency for New Technologies, Energy and Sustainable Economic Development (ENEA), Casaccia Research Centre, Via Anguillarese 301, 00123 Rome, Italy; marialuisa.grilli@enea.it

* Correspondence: sebab@uns.ac.rs; Tel.: +381-21-485-2339

Received: 6 March 2019; Accepted: 19 March 2019; Published: 15 May 2019



Abstract: Besides a wide application in corrosion protection, wear resistance increase, providing thermal properties and power conversion, oxide coatings have found an alternative application in welding technology as catalysts of the tungsten inert gas (TIG) welding process. In this paper, the novel approach of fabricating a coating containing nanoparticles based on nanosized SiO₂ and TiO₂ and their mixtures was applied to the austenitic stainless-steel base metal. It was found that coatings increased depths of penetration, enabling a consumable-free welding. Using this method, the use of several critical and near-critical raw materials (e.g., Si and Cr), as well as the relatively expensive Ni can be completely avoided. The most effective coating in terms of weld penetration consisted of a mixture of nanoparticles, rather than unary oxide coatings based on nanoparticles. A model for liquid weld metal flow is proposed based on the metallographic examination of recrystallized grains and microhardnesses measured near the weld metal, supporting the reversed Marangoni convection theory.

Keywords: oxide coating; nanoparticles; TIG welding; penetration depth

1. Introduction

The traditional form of oxide coatings has several purposes, mainly to protect the base material against corrosion [1–3] and wear [4–6], to obtain certain thermal properties [7,8], and to be used for power conversion [9,10]. However, a special type of metal-oxide coating can be used in welding technology with a high potential for application in the industrial sector.

One of the most widely used welding processes is gas tungsten arc welding (GTAW) or alternatively called tungsten inert gas (TIG). This process is well known for producing high-quality welds in different metals and alloys, most commonly for different types of stainless steels and non-ferrous alloys based on aluminum, copper, nickel, titanium, etc. [11–13]. Compared to the metal inert gas (MIG), which is used for welding a similar array of materials, TIG suffers from a lower productivity due to a lower welding speed and relatively low penetration, even in the case of currents when an excess of 300 A

is used [14]. The low productivity of TIG can be addressed by the introduction of a coating applied before welding over the surface to be welded to act as a catalytic agent of the welding process kinetics. This process is named activated tungsten inert gas (A-TIG). The first of such coatings was developed by Gurevich et al. during the 1960s at the Paton Welding Institute in Kiev, former USSR (now Ukraine). The coating—sprayed or applied by a brush—contains powdered metal oxides such as TiO_2 , Al_2O_3 , SiO_2 , NiO , MnO_3 , Cr_2O_3 , CeO_2 , and V_2O_5 [15–19], in ethanol, methanol, or acetone solvents [20]. The coated surface is usually approximately 0.15 mm thick [21]. As the highly volatile solvent is quickly dried, the welding will be started shortly after the application to the surface of the base metal. The welding arc can be started once the coating is dried, with the ultimate result of dramatically increased penetration depth (D) and narrowed weld width (W), achieving a D/W ratio that is close to 0.8 [22], compared to 0.2–0.3 without the coating [16,22]. Usually, nano-oxide particle-based coatings are more effective in achieving both higher penetration and D/W ratios, reaching values over 1 [17]. The most probable cause is a higher specific surface area of nanoparticles compared to the more conventional microparticles. One key mechanism is thought to be the reversal of Marangoni convection. Marangoni convection is driven by weld pool surface tension: fluids flow from areas where the surface tension is lower towards areas where it is higher. In conventional TIG welding, the flow is from the center of the weld pool towards the edges of the weld pool, influencing the occurrence of a wide and shallow weld. By reversing the molten metal flow in A-TIG, flow from the weld pool to the center of the weld occurs, resulting in a significantly narrower and deeper weld [23,24]. Another effect could be the result of the electronegativity of the metallic constituents of oxides. Therefore, Al-, Si-, and Ti-oxides have attracted significant interest in scientific circles [25–27].

There are multiple benefits of using oxide coatings in the A-TIG welding process: The time- and resource-consuming cutting of a V-groove (V-preparation, single V preparation) of the base metal can be avoided, and a simpler and cheaper closed square joint can be used (I-preparation) instead; instead of multi-pass welding, single-pass welding can be sufficient, resulting in significant savings of shielding gas, and there is no need to apply consumable materials in the form of wire rods or wires, therefore allowing a cost reduction of the welding process [20,28]. A special benefit is to avoid the consumption of welding filler material containing critical raw materials for the European Union (EU) [29]. In the case of austenitic stainless steels, some regularly appearing elements such as silicon metal are currently critical for the EU [29]. There are also some elements that were on the previous list of critical raw materials (CRMs) [30]. One example is chromium, which appears with the significant content of 18% and is no longer critical in accordance with the EU's list of critical raw materials [29], but is near-critical and may become critical again in the near future. Another example is nickel, which is important because of its relatively high cost.

In this work, the effects of unary Si and Ti nano-oxide coatings as well as binary coatings containing various ratios of Si and Ti nano-oxides were studied in view of the weld depth, width and D/W ratio, the phenomenology of the process, and the impact on CRMs and near-CRMs, to obtain multiple excellent properties or benefits for the TIG welding process.

2. Materials and Methods

In this study, welding was done on AISI 304 austenitic stainless-steel base metal with the following chemical composition: <0.03% C, 0.5% Si, 1.3% Mn, <0.008% S, 18.03% Cr, 0.003% P, 0.010% Al, 0.41% Cu, 9.51% Ni, 0.012% Sn and 0.07% V, with Fe making up the balance. The plates used for welding-re-melting were 10-mm-thick, were water-jet cut to 50 mm width and obtained from a single stainless-steel plate used as provided from the manufacturer, without any heat treatment.

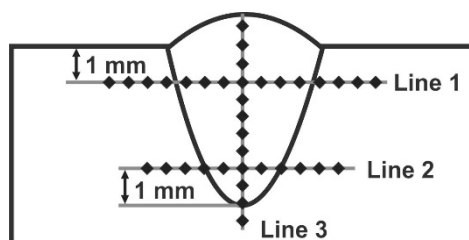
Overall, six different coatings were prepared using 20 nm TiO_2 and SiO_2 nanoparticles. Nanoparticles at 5 wt. % were mixed with acetone ($(\text{CH}_3)_2\text{CO}$), having a pH of 7, to produce a uniform mixture. Nanoparticles were weighed using a Tehtnica Type 2615 analytic balance (Zelevniki, Slovenia) and subsequently mixed with the solvent using a Tehtnica mm530 magnetic stirrer (Zelevniki,

Slovenia) for 10 min. To determine the size of the particles in the liquid component, a Zetasizer Nano ZS analyzer (Malvern Instruments, Malvern, UK) was used.

The coating was manually applied to the base material using a brush, coating in layers with a width of approximately 20 mm. The welded specimens, welded with various mixtures, were designated as: 5Si (100% SiO₂), 4Si1Ti (80% SiO₂; 20% TiO₂), 3Si2Ti (60% SiO₂; 40% TiO₂), 2.5Si2.5Ti (50% SiO₂; 50% TiO₂), 2Si3Ti (40% SiO₂; 60% TiO₂), 1Si4Ti (20% SiO₂; 80% TiO₂), and 5Ti (100% TiO₂). Specimen 0 was welded without the coating for the purpose of comparison and evaluation of the effects of coatings.

Welding was done using an EWM Tetrix 230 AC/DC welding power source (Mündersbach-Westerwald, Germany) with 200 A DCEN current and by the application of a 12.7 mm diameter nozzle. The electrode tip was sharpened to 90°. Tungsten with a 2% thorium electrode having a 2.4 mm diameter was used. The distance between the electrode tip and the base material was 2 mm, while the electrode was 6 mm out of the torch. Welding speed was 100 mm/min for all specimens. In specimen 0, the base metal was prepared using a 2-mm-deep V-groove with an angle of 90°. Consumable material in the form of a 0.8-mm coil wire made of AISI 308 ($\leq 0.08\%$ C; $\leq 2\%$ Si; $\leq 0.045\%$ P; $\leq 0.03\%$ S; $\leq 1\%$ Ni; 19%–21% Cr; 10%–12% Ni) was continuously added to the weld pool. Specimens welded with a coating were welded without the V-groove and consumable material.

The characterization of welds in order to evaluate the effectiveness of produced coatings comprised the following techniques: macro testing, microstructure examination, and microhardness, done in various weld areas (weld material, heat-affected zone, and base material). Macro and microstructural examination was done after a common metallographic preparation procedure consisting of the following: cutting, mounting into a 20 mm diameter polyethylene cup, grinding (using 150–2000 grit abrasive paper) and polishing (using 6, 3, 1, and 0.5 μm diamond suspension). Etching was done using aqua regia. Metallographic specimens were examined using a Leitz Orthoplan light microscope (Oberkochen, Germany), which was also used to measure the crucial weld dimensions (width— W and depth— D). Microhardness was measured using a Wilson Tukon 1102 (Uzwil, Switzerland) Vickers measurement device with a 1 kg load. Vickers microhardness measurement was done in parallel to the surface, 1 mm under it and 1 mm from the bottom of the weld metal. Microhardness was also measured through the weld metal, from the weld face to the bottom of the weld metal. The schematic depiction of the microhardness measurement is shown in Scheme 1.



Scheme 1. Microhardness measurement scheme.

3. Results

3.1. Particle Size Fractions

Particle size fractions are shown in Figure 1. In Figure 1, only fractions of up to 4 μm are shown, balance values of up to 17 μm were omitted to enable compactness of the chart. The largest number of particles were up to 1 μm , while larger fractions were progressively smaller as the particle size range was higher. This occurred in spite of the nominal nanoparticles that were used, indicating that intensive agglomeration was present. The fraction of particles having a size up to 1 μm was higher in all TiO₂ compared to all SiO₂ nanoparticle coating solvents, but the highest number of detected particles in this range was in coatings based on mixtures of SiO₂ and TiO₂ particles. The maximum particle size fraction was reached in specimen 2Si3Ti.

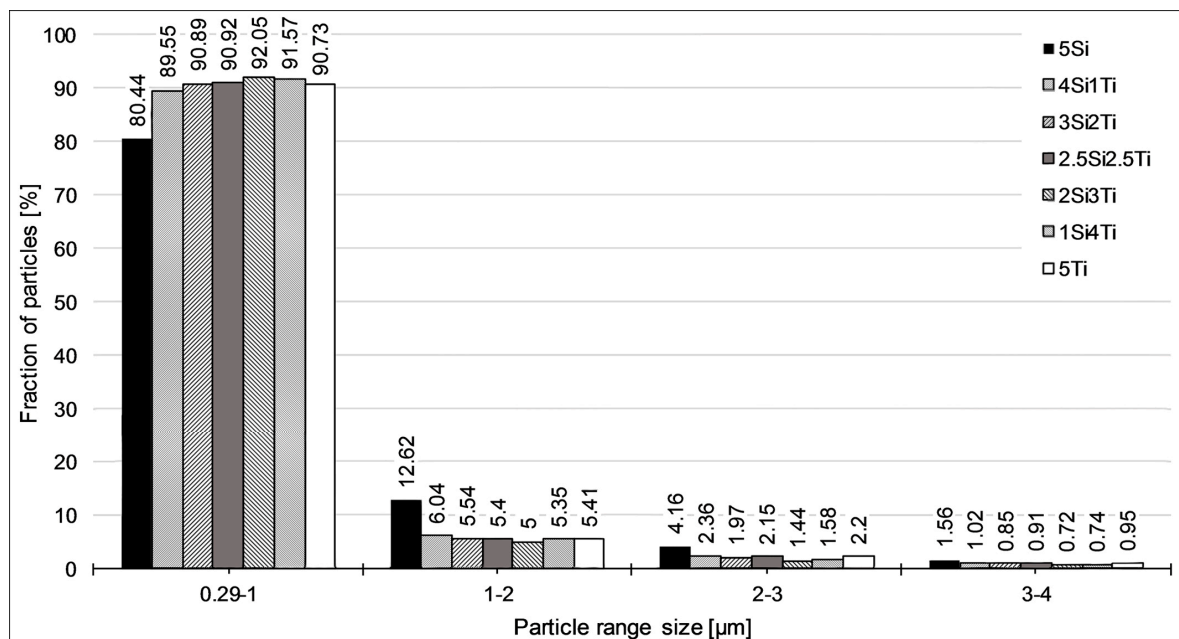


Figure 1. Zetasizer results.

3.2. Macro and Weld Bead Dimensions

Macro images of obtained weld beads are presented in Figure 2, along with the width (W), depth (D), depth-to-width ratios (D/W), and specimen designation. Weld bead measurements were averages of measurements taken from five macro images reported along with standard deviations. In Figure 2, both the conventionally welded–re-melted specimen (0) and specimens welded with the coating are shown. It can be seen that the introduction of the coating significantly influenced the melted profile of the weld. Firstly, the weld bead width decreased. It was roughly half of that of specimen 0's weld bead width. More importantly, weld depth was significantly increased. Specimen 5Si obtained with a SiO₂ nanoparticle coating had a lower penetration depth than 5Ti, obtained with a coating containing TiO₂ nanoparticles. The highest penetration was obtained with specimen 2Si3Ti. Deviations reported in Figure 2 were on the same order of magnitude for all specimens. There was no positive correlation between the increase in penetration and the narrowing of the weld, as for the depth-to-width ratios (D/W). However, D/W ratios increased from 0.28 in specimen 0 to 0.66 (specimen 2Si3Ti) and 0.79 (specimen 1Si4Ti) on average.

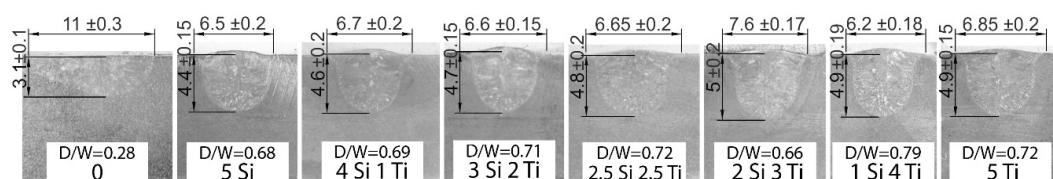


Figure 2. Macro images of specimens welded without (specimen 0) and with coating (specimens 5Si, 4Si1Ti, 3Si2Ti, 2.5Si2.5Ti, 2Si3Ti, 1Si4Ti, and 5Ti), with the indicated weld bead widths, penetration depth/width ratios (D/W), and standard deviations.

3.3. Microstructures

Microstructures identified within and near the melting line are shown in Figures 3–5. The analysis will mainly refer to the comparison between specimen 0, obtained without the coating and with consumable material, and specimens obtained with the coating and without consumable material. Weld metal microstructures of specimens 0, 4Si1Ti, 3Si2Ti, and 5Ti are shown in Figure 3. It can be seen that the microstructure was typically dendritic, a common feature for all the tested specimens.

Some differences appeared to exist, but they were the result of a different orientation of dendrites and various cross sections that were obtained.

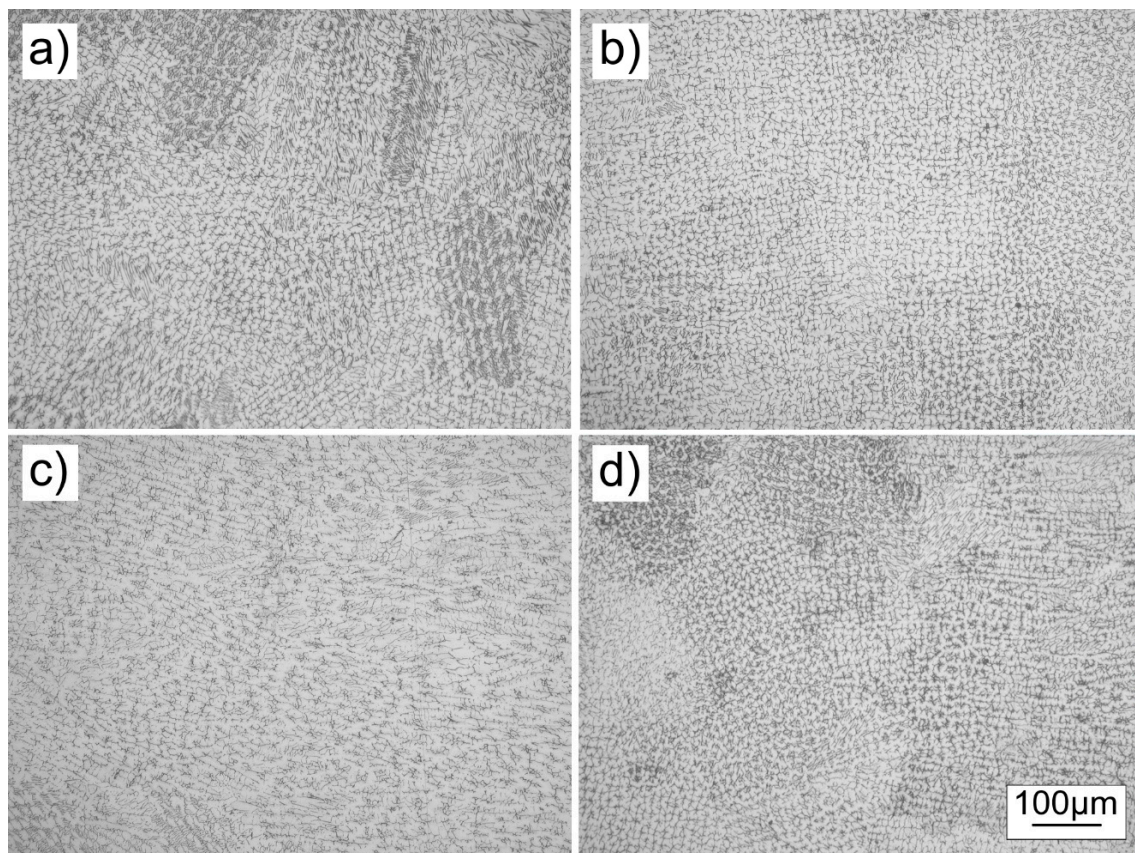


Figure 3. Microstructures of weld metals of specimens: (a) 0; (b) 4Si1Ti; (c) 3Si2Ti; (d) 5Ti.

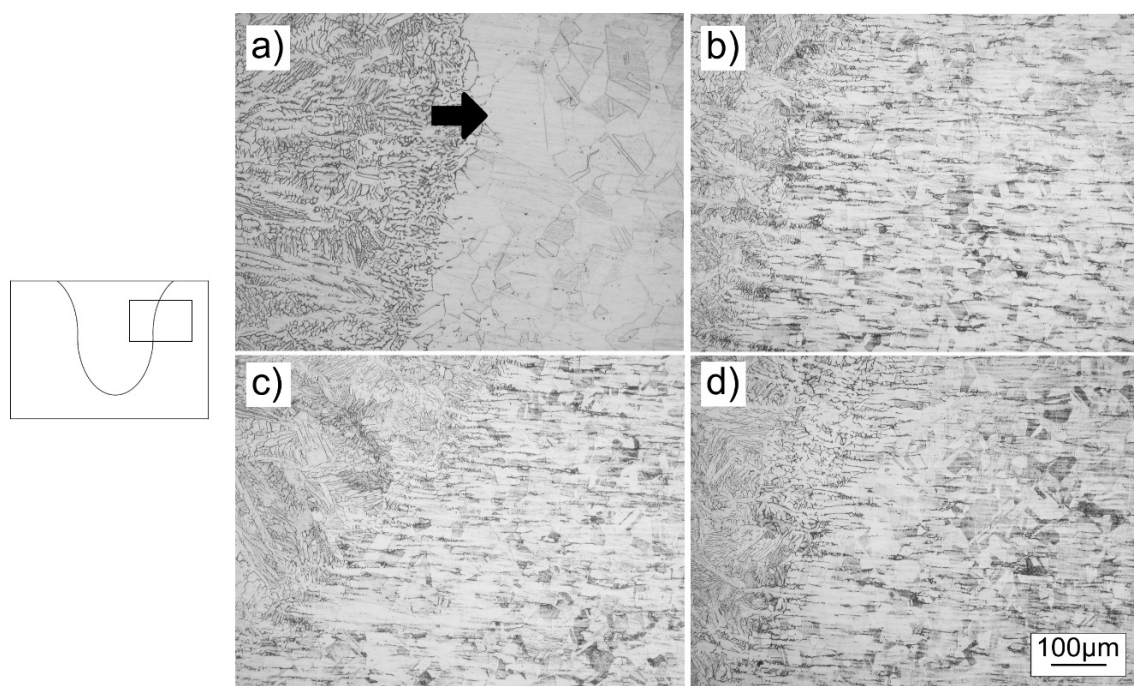


Figure 4. Microstructures under the surface of the specimen near the melt line: (a) specimen 0; (b) specimen 5Ti; (c) specimen 1Si4Ti; (d) specimen 2Si3Ti.

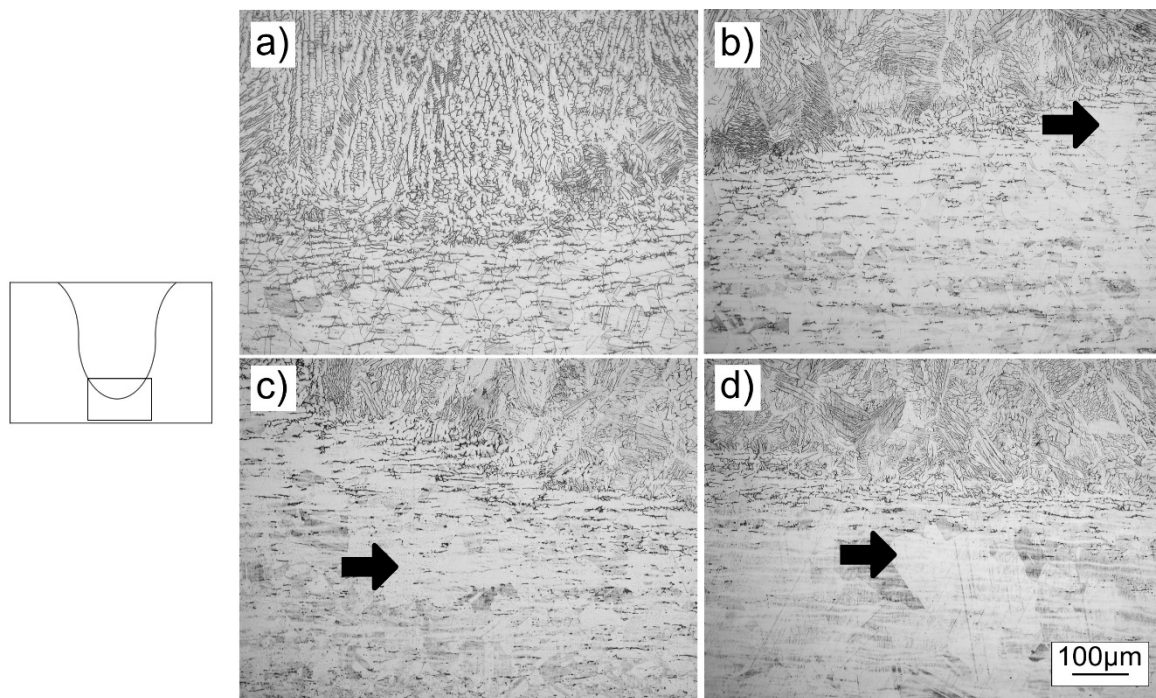


Figure 5. Microstructures under the weld metal near the melt line: (a) specimen 0; (b) specimen 5Si; (c) specimen 4Si1Ti; (d) specimen 2.5Si2.5Ti.

Microstructures in the base metal near the melt line under the surface of the material are shown in Figure 4. Specimens obtained without the coating (specimen 0) and with the coating (specimens 5Ti, 1Si4Ti, and 2Si3Ti) are shown with significant differences. The specimen obtained without the coating had significantly larger austenite polygonal grains in this area (Figure 4a, indicated by an arrow), which were not present in specimens obtained with the coating (Figure 4b–d).

Differences between microstructures under the weld of specimens 0, 5Si, 4Si1Ti, and 2.5Si2.5Ti are shown in Figure 5. It can be seen that, as in Figure 4, certain differences existed, consisting mainly of coarser grains observed in specimens obtained with the coating (Figure 5b–d, indicated by arrows) as compared to the specimen obtained without the coating (Figure 5a). Note that such a microstructure was not obtained directly under the weld metal, but rather slightly to the side.

3.4. Vickers Microhardness Results

The microhardness results are shown in Figures 6 and 7, while average values of the microhardness data measured in the weld metal are shown in Table 1. It can be seen that the major difference between welds obtained without (Figure 6a) and with the nanoparticle-based coating (Figure 6b–h) was in the microhardness values of the weld metals, as shown in Table 1. This was due to the application of a consumable welding wire. Additionally, based on the results shown in Figures 6 and 7 it can be seen that there were drops in microhardness occurring in the base metal near the melt line. However, there were differences between specimens obtained without and with the coating. Namely, in the specimen welded without the coating (0) drops in microhardness occurred in Line 1, right next to the weld line (Figure 6a, marked with black arrows). In specimens welded with coatings (Figure 6b–h) no such drop in microhardness was noted, but a similar drop in microhardness was observed right under the bottom of the weld (Figure 6b–h), which was not observed in the specimen welded without the coating (Figure 6a). The increased microhardnesses obtained in the weld metal were the result of the application of a consumable material in the form of a welding wire.

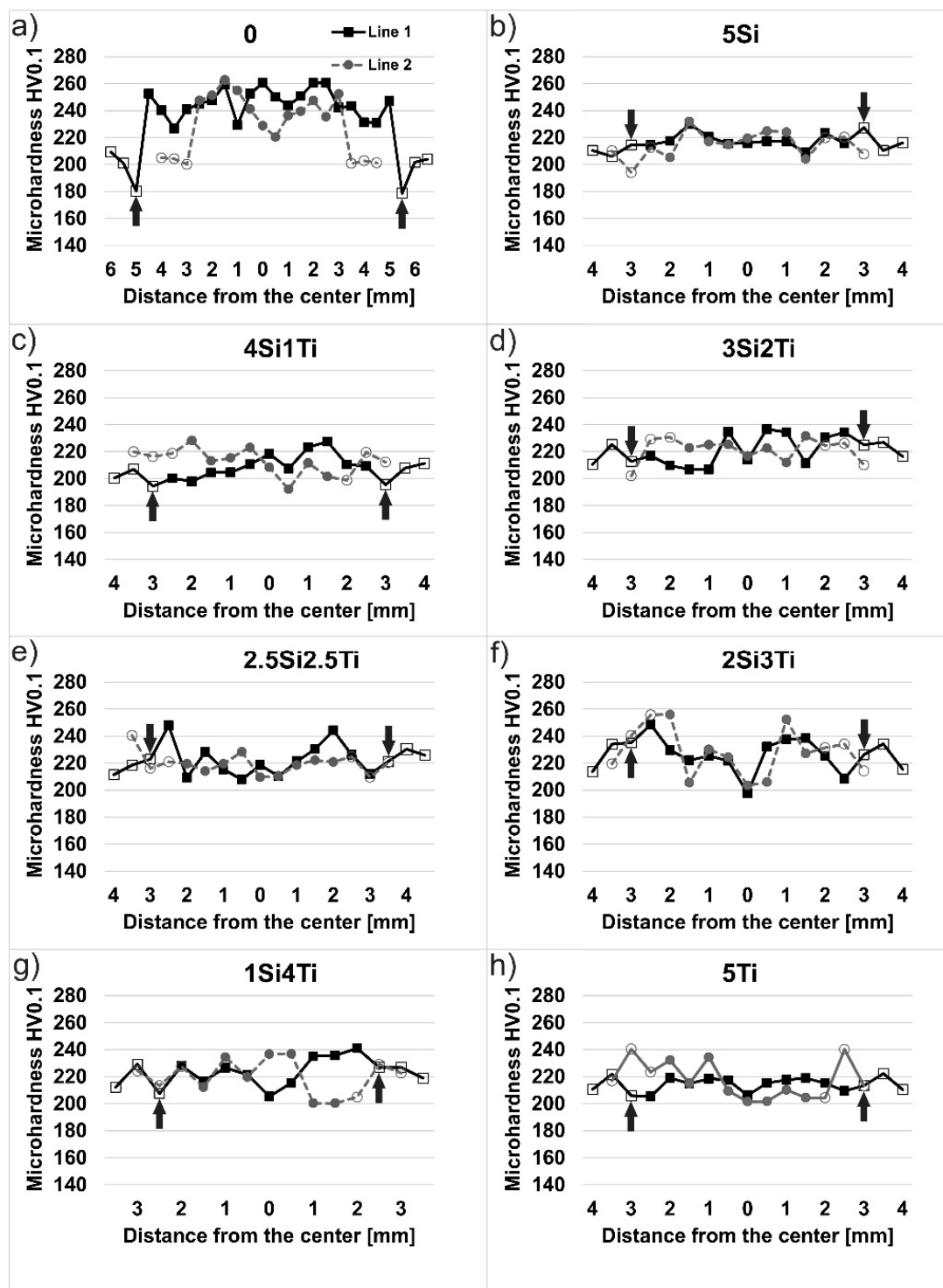


Figure 6. Microhardness values measured in Line 1 and Line 2: (a) specimen 0; (b) specimen 5Si; (c) 4Si1Ti; (d) 3Si2Ti; (e) 2.5Si2.5Ti; (f) 2Si3Ti; (g) 1Si4Ti; (h) 5Ti.

Table 1. Average microhardness values for Lines 1, 2, and 3 measured in the weld metal.

Measurement Area	0	5Si	4Si1Ti	3Si2Ti	2.5Si2.5Ti	2Si3Ti	1Si4Ti	5Ti
Line 1	246	218	210	221	223	226	225	214
Line 2	243	218	212	222	218	225	220	214
Line 3	245	215	214	220	221	227	223	212

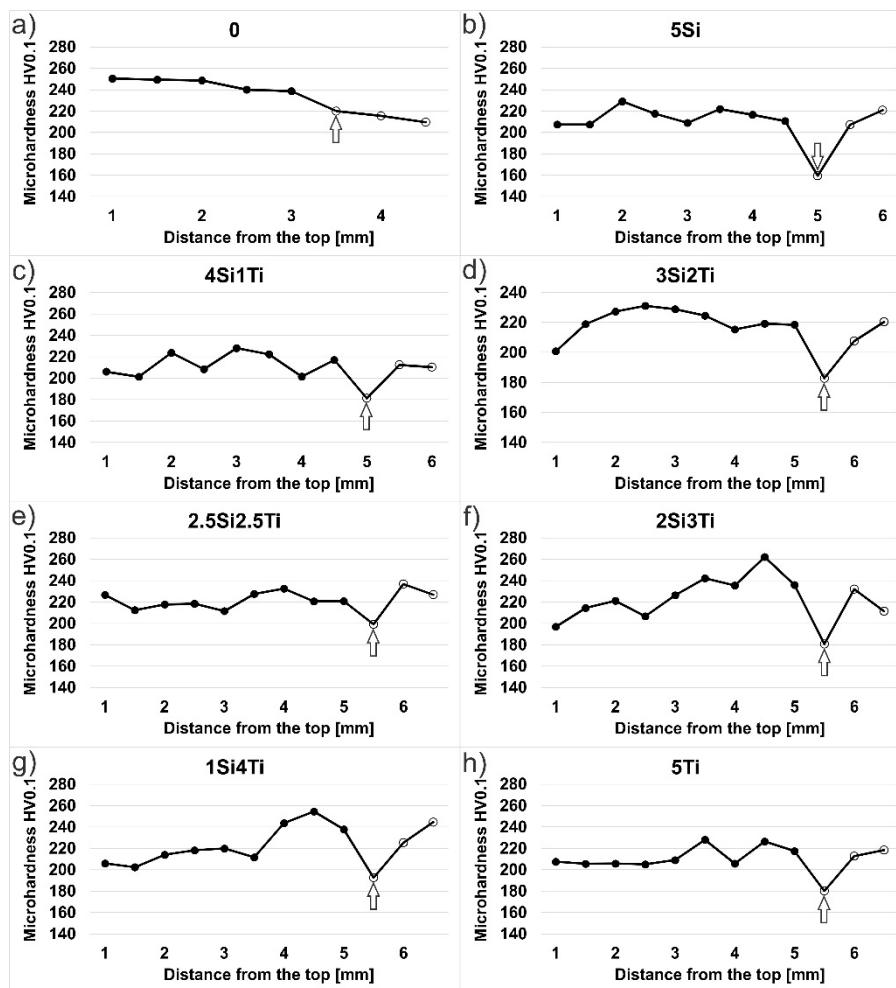


Figure 7. Microhardness values measured in Line 3: (a) specimen 0; (b) specimen 5Si; (c) 4Si1Ti; (d) 3Si2Ti; (e) 2.5Si2.5Ti; (f) 2Si3Ti; (g) 1Si4Ti; (h) 5Ti.

4. Discussion

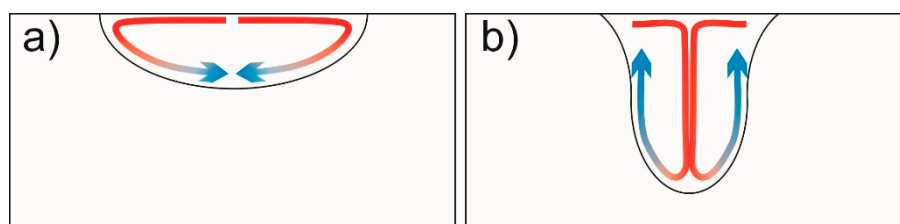
The application of a nanoparticle-based coating applied before the TIG welding had multiple effects. The first and most important was the increase in weld penetration, even though the welding without the coating applied was used with a welding wire and a relatively small V-groove. The increase in penetration was 61% in the case of the most effective mixture containing 2% SiO₂ and 3% TiO₂ nanoparticles, closely followed by 1% SiO₂ and 4% TiO₂ nanoparticles. Unary TiO₂ coatings proved clearly superior to SiO₂-based coatings. These results were not in agreement with the results obtained in studies by Venkatesan et al. [22,31], who found that a SiO₂-based coating was more effective compared to a TiO₂-based coating at the same welding parameters. The results obtained by Venkatesan et al. [22,31] could be explained by a higher electronegativity of Si (Pauling scale 1.9) versus Ti (Pauling scale 1.54) [20,32,33]. However, one possible explanation in the discrepancy between this study and studies by Venkatesan et al. [22,31] is the size of oxide particles in the coating. Namely, when mixed with the solvent (i.e., acetone), the results suggested that particle agglomeration of TiO₂ was more favorable towards a smaller size compared to SiO₂. A higher amount of relatively small particles in the flux can be well correlated to a higher effectiveness of a TiO₂-based coating compared to a SiO₂ one. Microparticles have a lower tendency to agglomerate [34], and therefore electronegativity in A-TIG welding on penetration depth can be of greater importance.

The most convenient particle size distribution was obtained with mixtures of SiO₂ and TiO₂ nanoparticles, most particularly 2Si3Ti, which closely corresponded to the highest penetration of the

specimen obtained with the application of this particular coating. These results are in accordance with the results obtained by Venkatesan et al. [22,31], who also obtained the highest penetration not with single-component coatings, but rather with mixtures—particularly the SiO_2 and TiO_2 metal-oxides, which were also used in our study.

When nanoparticles are used, as in the case of the present study, it must be noted that the nanoparticle nominal size cannot be considered as influential. Rather the distribution of nanoparticles in accordance to their size is of utmost importance, which accounts for the occurrence of nanoparticle agglomeration, the sizes of which were measured by a Zetasizer in the present study. The results observed with nanoparticle mixtures could be the result of a lower tendency to agglomerate—that is, a higher amount of relatively small particles agglomerates with size up to $1\text{ }\mu\text{m}$. A similar result regarding a lower tendency to form agglomerates with nanoparticle mixtures was obtained by Efimov et al. [35].

The results of penetration suggest a significant advantage of the application of coatings for TIG welding versus the preparation with an applied consumable wire. The main mechanism of the increased penetration depth was the reversal of the Marangoni convection, proved by the microstructural study. The material flow model with molten metal temperature indicators are shown in Scheme 2. In the specimen welded without the coating (specimen 0), the material flowed from the center of the molten surface towards the melting lines and then towards the bottom and back to the centerline. In this process, the heat was dissipated mainly to the base metal on the sides. This means that the highest heat transfer was towards this area, which caused recrystallization and grain growth, as documented by the microstructure shown in Figure 4a (recrystallization in the horizontal plane). The unchanged microstructure under the weld suggests that the heat transfer towards this area was much less intensive, which is understandable since the melt dissipated its heat to the sides, next to the weld. This was proved by the microhardness measurements with minimum values obtained in this area (Figure 6a). On the other hand, a reversed Marangoni convection caused the material to flow inwards and towards the bottom of the weld, increasing penetration, as well as heat transfer under the weld into the base metal. This means that the area under the weld received the most heat, which resulted in the austenite grain growth—that is, recrystallization in the vertical plane (Figure 5b–d). Similarly to the specimen obtained without the coating, specimens with the applied coating showed a marked drop in microhardness under the weld (Figure 7b–h).



Scheme 2. Material flow model: (a) without the coating; (b) with the coating.

Recrystallization in the horizontal plane that occurred in TIG without the coating was less convenient, weakening the material perpendicular to the weld, unlike the recrystallization in the vertical plane in A-TIG with a truly multifunctional coating. This means that three crucial benefits are obtained with the application of coatings:

1. Improved penetration, along with all accompanying benefits of a lower shielding gas consumption, an increased productivity, a lower environmental impact, and lower costs;
2. A lower negative influence on the material's microstructure and subsequently higher tensile strength, which is proportional to the hardness of the material;
3. A completely eliminated consumable material (i.e., welding wire) containing CRMs such as silicon and a near-CRM such as chromium.

However, special attention must be paid to the root of the weld, keeping in mind that the material flow and its heat transfer was to the bottom part of the weld metal, reducing viscosity and increasing the tendency of the molten metal to flow, causing over-penetration.

5. Conclusions

Based on the results presented in this work, the following conclusions can be drawn:

- Coatings containing metallic oxide nanoparticles offer a higher A-TIG welding penetration compared to the specimen without the coating;
- The added consumable material in TIG results in a higher hardness of the weld metal compared to the specimens that were re-melted—that is, welded without the consumable material (A-TIG);
- The penetration of A-TIG specimens depends primarily on the particle size in the coating solution, not the primary particle size, due to the agglomeration of nanoparticles;
- smaller size of agglomerates in coatings with an increased TiO_2 content caused a higher coating effectiveness, leading to an increased penetration that reached a value of 61% over that of the TIG weld without the coating;
- The presence of the reversed Marangoni convection was proved by the recrystallization of certain areas of the base metal near the melt line: near the surface in TIG specimen and under the weld in A-TIG specimens. These results were proved by microhardness measurements, with marked drops in microhardness values in recrystallized areas.

An A-TIG coating based on metallic oxide nanoparticles acting as catalysts for welding process gives several benefits to the resulting weld: improves technological properties and improves environmental friendliness (higher penetration, lower shielding gas consumption, improved productivity, etc.), mechanical integrity (weak parts in A-TIG specimens are theoretically under the weld rather than to the sides) and finally, a complete elimination of CRMs and near-CRMs such as Si and Cr, respectively. On the other hand, the catalytic activity of the coating may cause over-penetration as the high-temperature molten metal flows directly downwards, towards the weld root.

Author Contributions: S.B. designed the experiment and wrote the paper; M.D. and P.J. performed the experiments; I.Z. provided the resources (devices, materials); D.K. and M.B. interpreted the data, and reviewed and edited the manuscript; M.L.G. provided work administration and supervision.

Funding: This research received no external funding.

Acknowledgments: This article is based on work from COST Action “Solutions for Critical Raw Materials under Extreme Conditions”, supported by COST (European Cooperation in Science and Technology).

Conflicts of Interest: The authors declare no conflict of interest.

References

1. Gulicovski, J.J.; Bajat, J.; Miskovic-Stankovic, V.; Jokic, B.; Panic, V.; Milonjic, S. Cerium oxide as conversion coating for the corrosion protection of aluminum. *J. Electrochem. Sci. Eng.* **2017**, *3*, 151–156. [[CrossRef](#)]
2. Bieber, J. Trivalent chrome conversion coating for zinc and zinc alloys. *Mater. Lett.* **2007**, *105*, 425–435.
3. Ana-Maria, L.; Wolfgang, P.Y.; Sabrina, M.; Nadine, P.; Diane, S.; Tendero, C.; Vahlas, C. Corrosion protection of 304L stainless steel by chemical vapour deposited alumina coatings. *Corros. Sci.* **2014**, *81*, 125–131.
4. Cellarda, A.; Garniera, V.; Fantozzia, G.; Bareth, G.; Fort, P. Wear resistance of chromium oxide nanostructured coatings. *Ceram. Int.* **2009**, *35*, 913–916. [[CrossRef](#)]
5. Hwanga, B.; Leea, S.; Ahn, J. Effect of oxides on wear resistance and surface roughness of ferrous coated layers fabricated by atmospheric plasma spraying. *Mat. Sci. Eng. A* **2002**, *335*, 268–280. [[CrossRef](#)]
6. Fomin, A.A.; Rodionov, I.V. *Handbook of Nanoceramic and Nanocomposite Coatings and Materials*, 1st ed.; Butterworth-Heinemann: Oxford, UK, 2015; pp. 403–424.
7. Curran, J.A.; Clyne, T.W. The thermal conductivity of plasma electrolytic oxide coatings on aluminium and magnesium. *Surf. Coat. Technol.* **2005**, *199*, 177–183. [[CrossRef](#)]

8. Narottam, P.B.; Dongming, Z. Thermal Properties of Oxides with Magnetoplumbite Structure for Advanced Thermal Barrier Coatings. *Surf. Coat. Technol.* **2008**, *202*, 2698–2703.
9. Calnan, S. Applications of Oxide Coatings in Photovoltaic Devices. *Coatings* **2014**, *4*, 162–202. [[CrossRef](#)]
10. Sang, Y.J.; Jaesun, S.; Sanghan, L. Photoelectrochemical Device Designs toward Practical Solar Water Splitting: A Review on the Recent Progress of BiVO₄ and BiFeO₃ Photoanodes. *Appl. Sci.* **2018**, *8*, 1388–1404.
11. Thakur, P.P.; Chapgaon, A.N. A Review on Effects of GTAW Process Parameters on weld. *IJRASET* **2016**, *4*, 136–140.
12. German Development Service-GIZ, Gas Tungsten Arc Welding-GTAW. 2000. Available online: <https://www.giz.de/expertise/downloads/Fachexpertise/en-metalwork-gas-tungsten-arc-welding.pdf> (accessed on 15 March 2019).
13. Cibi, A.J.; Thilagham, K.T. High Frequency Gas Tungsten Arc Welding Process for Dressing of Weldment. *IJAERS* **2017**, *4*, 229–235.
14. Robert, W.; Messler, J. *Principles of Welding: Processes, Physics, Chemistry, and Metallurgy*; Wiley-VCH: Weinheim, Germany, 2004; p. 55.
15. Ramkumar, K.D.; Goutham, P.S.; Radhakrishna, V.S.; Tiwari, A.; Anirudh, S. Studies on the structure–property relationships and corrosion behaviour of the activated flux TIG welding of UNS S32750J. *Manuf. Process.* **2016**, *23*, 231–241. [[CrossRef](#)]
16. Yangchuan, C.; Zhen, L.; Zunyue, H.; Yida, Z. Effect of cerium oxide flux on active flux TIG welding of 800 MPa super steel. *J. Mater. Process. Technol.* **2016**, *230*, 80–87.
17. Vora, J.J.; Badheka, J.B. Experimental investigation on mechanism and weld morphology of activated TIG welded bead-on-plate weldments of reduced activation ferritic/martensitic steel using oxide fluxes. *J. Manuf. Process.* **2015**, *20*, 224–233. [[CrossRef](#)]
18. Jurica, M.; Kozuh, Z.; Garasic, I.; Busic, M. Optimization of the A-TIG welding for stainless steels. *IOP Conf. Ser. Mater. Sci. Eng.* **2018**, *329*, 1–9. [[CrossRef](#)]
19. Klobcar, D.; Tusek, J.; Bizjak, M.; Simoncic, S.; Lešer, V. Active flux tungsten inert gas welding of austenitic stainless steel AISI 304. *METABK* **2016**, *55*, 617–620.
20. Vidyarthi, R.S.; Dwivedi, D.K. Activating flux tungsten inert gas welding for enhanced weld penetration. *J. Manuf. Process.* **2016**, *22*, 211–228. [[CrossRef](#)]
21. Vora, J.J.; Badheka, J.B. Improved Penetration with the Use of Oxide Fluxes in Activated TIG Welding of Low Activation Ferritic/Martensitic Steel. *Trans. Indian Inst. Met.* **2016**, *69*, 1755–1764. [[CrossRef](#)]
22. Venkatesan, G.; George, J.; Sowmysari, M.; Muthupandi, V. Effect of ternary fluxes on depth of penetration in A-TIG welding AISI 409 ferritic stainless steel. *Procedia Mater. Sci.* **2014**, *5*, 2402–2410. [[CrossRef](#)]
23. Takeuchi, Y.; Takagi, R.; Shinoda, T. Effect of bismuth on weld joint penetration in austenitic stainless steel. *Weld. Res. Suppl.* **1992**, *71*, 283–290.
24. Mills, K.C.; Keene, B.J.; Brooks, R.F.; Shirali, A. Marangoni effects in welding. *Philos. Trans. R. Soc. A Math. Phys. Eng. Sci.* **1998**, *356*, 911–925. [[CrossRef](#)]
25. Skvortsov, E.A. Role of electronegative elements in contraction of the arc discharge. *Weld Int.* **1998**, *12*, 471–475. [[CrossRef](#)]
26. Tanaka, M.; Shimizu, T.; Terasaki, T.; Ushio, M.; Koshiishi, F.; Terasaki, H. Effects of activating flux on arc phenomena in gas tungsten arc welding. *Sci. Technol. Weld Join.* **2000**, *5*, 397–402. [[CrossRef](#)]
27. Kuang-Hung, T.; Po-Yu, L. UNS S31603 Stainless Steel Tungsten Inert Gas Welds Made with Microparticle and Nanoparticle Oxides. *Materials* **2014**, *7*, 4755–4772.
28. International Standard ISO 9692-1:2013. *Welding and Allied Processes—Types of Joint Preparation—Part 1: Manual Metal-arc Welding, Gas-Shielded Metal-arc Welding, Gas Welding, TIG Welding and Beam Welding of Steels*; ISO: Geneva, Switzerland, 2013.
29. EUROPEAN TYRE & RUBBER MANUFACTURERS' ASSOCIATION. Available online: <http://www.etrma.org/uploads/Modules/Documentsmanager/20170913---2017-list-of-critical-raw-materials-for-the-eu.pdf> (accessed on 24 November 2018).
30. Report on Critical Raw Materials for EU, Report of the Ad-Hoc Working Group on Defining Critical Raw Materials for EU. May 2014. Available online: http://mima.geus.dk/report-on-critical-raw-materials_en.pdf (accessed on 24 November 2018).
31. Venkatesan, G.; Muthupandi, V.; Justine, J. Activated TIG welding of AISI 304L using mono- and tri-component fluxes. *Int. J. Adv. Manuf. Technol.* **2017**, *93*, 329–336. [[CrossRef](#)]

32. Housecroft, C.E.; Sharpe, A.G. *Inorganic Chemistry*, 2nd ed.; Pearson, Prentice Hall, Pearson Education Limited: Edinburgh, UK, 2005; p. 38.
33. Tseng, K.H.; Chen, K.L. Comparisons between TiO_2 - and SiO_2 -flux assisted TIG welding processes. *J. Nanosci. Nanotechnol.* **2012**, *12*, 6359–6367. [[CrossRef](#)] [[PubMed](#)]
34. Trunec, M. Dispersion of nanoparticles in solvents, polymer solutions and melts, principles and possibilities. In Proceedings of the COST Action MP0701 Workshop, Novi Sad, Serbia, 23–24 September 2010.
35. Efimov, A.; Lizunova, A.; Sukharev, V.; Ivanov, V. Synthesis and Characterization of TiO_2 , Cu_2O and Al_2O_3 Aerosol Nanoparticles Produced by the Multi-Spark Discharge Generator. *Korean J. Mater. Res.* **2016**, *26*, 123–129. [[CrossRef](#)]



© 2019 by the authors. Licensee MDPI, Basel, Switzerland. This article is an open access article distributed under the terms and conditions of the Creative Commons Attribution (CC BY) license (<http://creativecommons.org/licenses/by/4.0/>).